5 Probing of Nanocontacts Inside a Transmission Electron Microscope

Donats Erts[1], Ants Lohmus[2], Justin D. Holmes[3], and Hakan Olin[4]

[1] Institute of Chemical Physics, University of Latvia, Riga, Latvia
[2] Institute of Physics, University of Tartu, Tartu, Estonia
[3] University College Cork, Cork, Ireland
[4] Mid-Sweden University, Sundswall, Sweden

5.1 Introduction

This chapter reviews a recent new method, which is a combination of the scanning probe microscope (SPM) and the transmission electron microscope (TEM), with important applications in nanotribological investigations of contact properties. In these TEM-SPM instruments, the electron microscope is used for imaging and analysis of the sample as well as the SPM tip, while the SPM is used for probing of the electrical and mechanical properties, measurements of force interaction or for manipulation of the sample at the nanometer scale. One advantage with the TEM-SPM instrument, compared with standard SPM, is the direct imaging of both tip and sample giving important information such as tip-sample distance, tip and sample radius and shape, which is lacking or only available indirectly using standard SPM.

The first TEM-SPM instrument, introduced by Spence [1], was a combination of the scanning tunnelling microscope (STM) and a TEM. While this early instrument was used for STM imaging, other groups later used TEM-STM instruments for probing and manipulations. Examples of their use can be illustrated by the creation of atomically thin gold nanowires and simultaneous conductance measurements by the group of Takayanagi [2], studies of the mechanical properties of carbon nanotubes by Poncharal et al. [3], the low friction linear bearing realized by carbon nanotubes by Cumings and Zettl [4], the investigations of conductance of gold point contacts by Erts et al. [5], and studies of electromigration of metal inside and outside carbon nanotubes [6,7]. The family of in situ probe instruments is growing and work is progressing on the atomic force microscopes (AFM) [8–11] and nanoindenters [12–14]. The body of applications of this young technique is expected to grow with the appearance of commercially available instruments [15].

5.2 TEM-SPM Instruments

One challenge in the design of a TEM in situ probe instrument is the short distance between the pole pieces (2 – 10 mm) of the objective lens where the sample is placed. The standard TEM side entry sample holder, roughly a 20 cm

long cylinder with a diameter of less than 1 cm with the sample placed at one end, is inserted into the TEM column.

The simplest, single directional TEM-SPM prototype device can be designed on the base of commercially available TEM specimen goniometre type holder. It is improved by a specimen support disc with slit perpendicular to main axes [16]. One part of the disc is fixed to the base cartridge and other to the movable part. The sample, laser-ablated nanoparticle aggregates, were deposited on the specimen disc. Due to a big plastic deformation of the disc material the slit can be enlargened without breaking the disc when tension is applied. The origin of the elastic behaviour of the nanoparticle chain aggregates were studied using this device.

In the TEM-SPM designs the scanning probe part is placed at the sample position. The most common sample is a tip-formed sample in order not to shadow the electron beam. The two main parts in a scanning probe microscope are the piezo- scanner with a range of a few micrometers and a rough positioning system, which is necessary to reduce the probe-sample distance within the reach of the piezo-scanner. While the standard piezo scanner is a tube with a diameter of a few mm, the rough positioning system is usually bulkier.

5.2.1 TEM-STM

TEM-SPM, based on micromechanical techniques [17], has significant advantages in achieving ultra-low noise measurements in comparison to standard SPM. Due to very small dimensions, only 2.5 by 2.5 by 0.5 mm, the resonance frequency is high. Such dimensions allow the use of very high resolution pole pairs in TEM. However due to the difficulties of making such an instrument in common laboratories and complications arising from manipulation of the sample under study this device has not found wide use.

One common way for TEM-STM design [1,8,18] is based on an electrical motor with a long shaft to displace a piezo element into operating range. Such a design [8] with a piezo tube scanner and a geared stepper motor is shown in Fig. 5.1a. This design is simple and robust; however, one disadvantage is the lack of rough motion in lateral directions. The lack of lateral positioning capability results in frequent misalignments between the tip-shaped sample and the probing tip during the coarse approach, leading to necessary manual readjustment outside the TEM.

An elegant design, using a single piezo tube both for fine motion and for 3-dimensional rough adjustment, is shown in Fig. 5.1b [8,19]. The rough motion is based on an inertial slider mechanism. A saw-tooth voltage applied simultaneously on piezotube electrodes enables a shift along a straight line. For lateral motions only a pair of electrodes will be used resulting in a tilt of the tip. The approach of the tips can be carried out step by step: by shifting the movable element- tip holder and by correcting the direction under TEM observation.

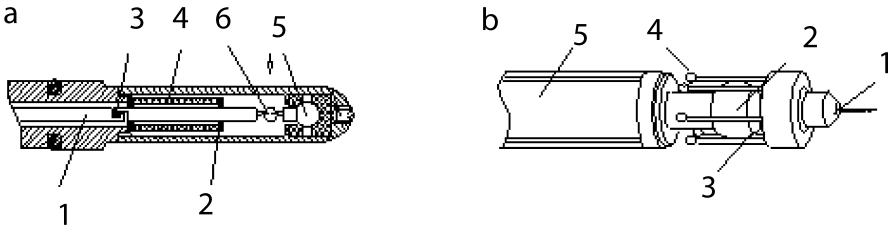

Fig. 5.1. TEM-SPM designs **a** Stepper motor based TEM-holder (not to scale): 1 – shifting rod by stepper motor, 2 – graphite rings, 3 – clutch, 4 – piezo tube, 5 – preadjustment ball, 6 – electron beam. **b** Ball-type of the inertial slider: 1 – tip holder, 2 – sapphire ball, 3 – sliding rods, 4 – counter weight, 5 – piezo tube

5.2.2 TEM-AFM

In the simplest version of TEM-AFM one tip, opposite to the piezo one is replaced with the AFM cantilever with a tip on it. If the standard AFM technique involves a cantilever and optical system for detecting the cantilever deflection then in TEM instead of the optical system the cantilever image is used for detecting the displacement of the tip [8, 9]. Kizuka [10, 11] used also optical detector for cantilever position control.

We have developed a TEM-AFM for shear force measurements based on a quartz resonator tuning fork inside the TEM. Friction increases rapidly as the distance between objects is reduced below 10 nm [20]. The instrument allows simultaneous turning and measurement of several parameters (frequency, amplitude, phase, sample potential, distance between nanoobjects, shear force damping, contact current, etc) while directly observing the system behaviour in TEM. An electronic module has been developed and integrated in the SPM controller. It consists of a frequency synthesizer, with frequencies tunable in 0.02 Hz steps, which can operate up to 10 MHz, and a lock-in amplifier for measurements of dissipated energy in the resonator.

5.2.3 In Situ Nanoindenter

The nanoindentation technique utilizes an actuator to press a sharp diamond tip a few nanometers into the sample while measuring the applied force, typically giving information about the hardness or elastic modulus of the material in the sub-micron regime. The data obtained by the nanoindentation method has been limited to load - displacement data and, by the lack of direct observation of the induced plastic deformation, to ex situ studies of the analysis of the indentation mark. Recently, however, an extension of the nanoindentation method has been demonstrated, using a TEM for in situ imaging of the entire indentation process [12–14]. To take full advantage of the TEM-nanoindentation method a proper force sensor is needed. Such a force sensor, fabricated by micromachining methods, is described in [13].

5.3 Force Interactions

TEM-AFM has a great potential for in situ observations of all force interaction. Nevertheless only few investigations of force interactions have been measured between Si, Cu and Au surfaces and between semiconductor nanowires and gold [9–11,21]. Figure 5.2 shows a typical sequence of TEM images where the Au sample with a protrusion of radius of 7.6 nm is moved towards and then away from the Au coated AFM tip of radius of 30 nm [9]. The corresponding force curve is found in Fig. 5.3.

5.3.1 Van der Waals Forces

Van der Waals forces can be determined by visualisation of the AFM tip positions before and after the jump to contact (Figs. 5.2 and 5.4) and calculating the force using the cantilever spring constant (Figs. 5.3 and 5.5).

A simple expression for the jump to contact, using a model with van der Waals forces between two spheres is [22]:

$$k < \frac{\mathrm{d}F}{\mathrm{d}s} = \frac{AR}{3s^2}\,, \tag{5.1}$$

where A is the Hamaker constant, s is the distance between the spheres, and R is the reduced radius of the spheres R_1 and $R_2 : R = ((R_1 + R_2)/R_1R_2)^{-1}$.

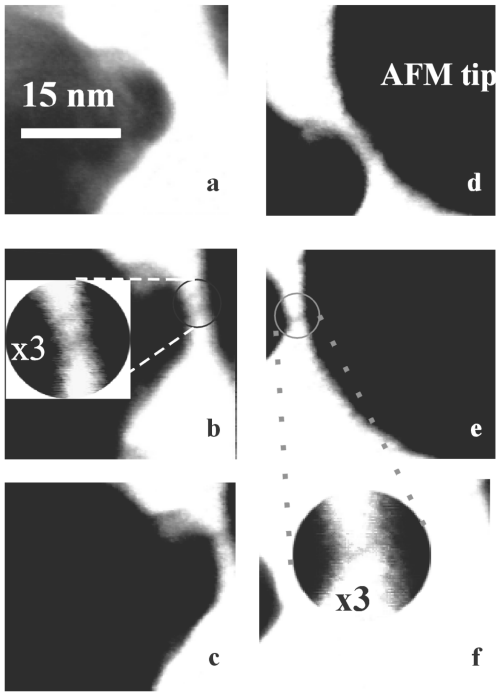

Fig. 5.2. A set of TEM images of a gold tip and gold coated AFM tip: **a** No contact. **b** Jump-to-contact. (Inset: neck formed in the gap in connection during the jump-in-contact event) **c** Moving further in. **d** Withdrawal of the sample. **e** By lateral motion of the sample a small nanowire is formed between the sample and tip. Just before breaking, the diameter of the wire is about 1 nm, which corresponds to about 10 atoms. **f** After jump-off-contact. (Inset: nanowire area magnified 3 times). Reproduced with permission from *Appl. Surf. Sci.* **2002,** 188, 460, Copyright 2002 Elsevier North-Holland

TS[f] Fig. 5.2?

Editor's or typesetter's annotations (will be removed before the final TEX run)

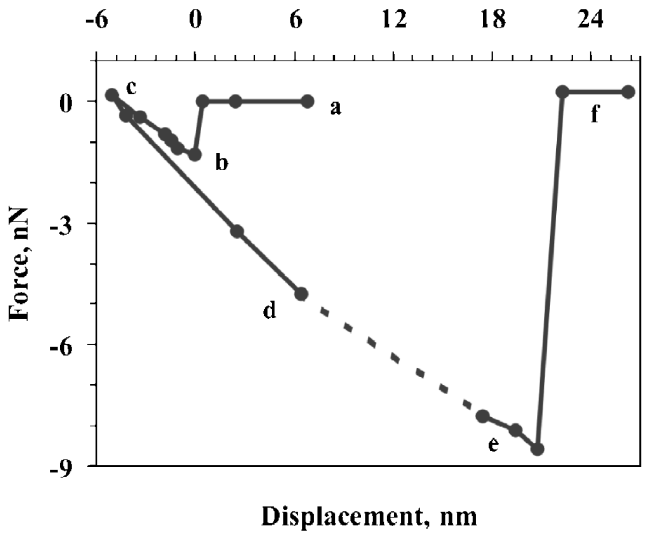

Fig. 5.3. Experimental force-distance curve where the labels a–f corresponds to the TEM images in Fig. 5.4a–f[rs f]. Reproduced with permission from *Appl. Surf. Sci.* **2002,** 188, 460, Copyright 2002 Elsevier North-Holland

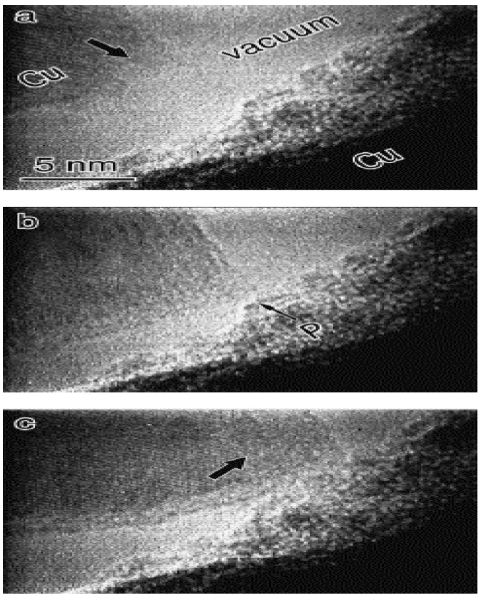

Fig. 5.4. TEM image snapshots of tip and surface, **a** before the tip contacts the surface; **b** just as the tip contacts the surface; **c** after the tip contacts, showing lateral displacement on the surface [11]

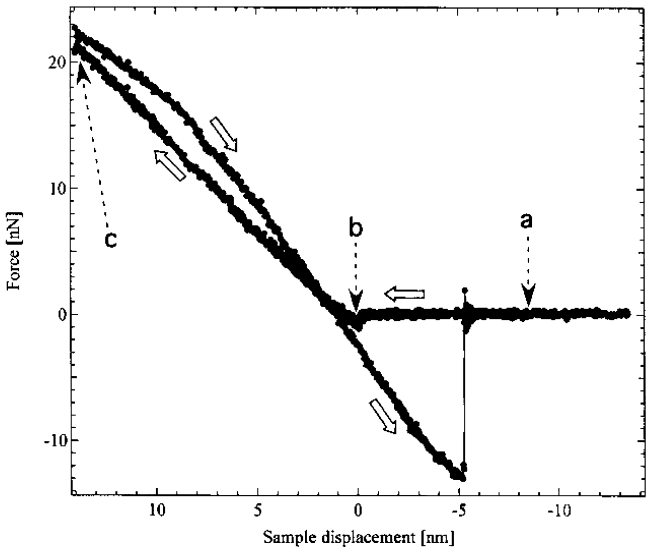

Fig. 5.5. Force-displacement curves for Cu tip and Cu surface [11]

Jump-to-contact distances shown in Fig. 5.2 are more than 20 times lower in comparison to those calculated using the cantilever spring constant. Such difference may be explained by the high mobility of the gold atoms in the gap between the two tips at room temperature when the static view might not be relevant.

One of conclusions from measurements of nanowires and nanotubes by TEM-STM is that both of them can be used as sensitive force sensors. The force constant of free standing Si and Ge nanowires is compatible to the AFM cantilever force constants. Measurements of the jump to contact for Si and Ge nanowires [21] have been used to determine force constant of nanowires.

5.3.2 Pull off Forces

With great success TEM-AFM can be used for the characterization of adhesion forces by visualization of contacts during the retraction process [9–11]. Figures 5.2c–f and 5.3 shows an example of the force measurement and TEM image of a nanowire with a diameter of less than 1 nm and length of 2 nm (Fig. 5.2e and inset) [9]. The nanowire was created from the larger diameter contact by shear force by a lateral motion of the sample (Fig. 5.2d,e). The nanowire broke at a retraction of 22 nm (Fig. 5.2e,f) which corresponds to an attractive force of about 9 nN (Fig. 5.3). The calculated cohesion force was approximately 1 nN per atom which is in agreement with gold nanowire force experiments (1.6 nN for the last atom) [23] as well as theoretical calculations (from 1 to 2.2 nN) [24].

Kizuka [10] measured the tensile strength, strain-stress force and conductivity at the same time for a gold nanowire breaking. The strain-stress curve exhibits a swath edge curve, indicating that the deformation proceeds by the repeated process of elastic elongation and slip. Oscillations were observed in the strain-stress curve before fracture. The yield stress is determined and is ≈ 8 GPa.

One more application is measurement of the strength of a junction between a carbon nanotube and gold created by Jeoule heating [25].The strength of contact is estimated from the critical bending of the cantilever at the fracture and is approximately 0.6 MPa. This strength is similar to the exfoliation strength of the graphite layers 0.4 MPa.

5.3.3 Shear Forces, Friction

Kizuka [10, 11] observed a frictional movement of the AFM tip during approach and the first contact to the surface between Au, Cu and oxide coated Si surfaces (Fig. 5.6). A hysteresis loop in the force-distance curves caused by frictional movement of the tip at the contact region is observed [11] (Fig. 5.5). Lateral frictional displacement of the tip on the sample surface along the cantilever in the contact state (Fig. 5.6) is observed by the TEM (Fig. 5.4). Frictional displacements on the surface just after the contact may achieve 5 nm and more and no contacts without sliding were observed. The tip slides in along the opposite direction due to the retraction and the tip position returns to its initial contact position [10]. It is shown that the lateral displacement is not constant but changes with normal load, which is very important for interpretation of friction data, especially on an atomic scale [11]. For oxide coated Si surfaces the contact boundary of silicon oxide was hardly deformed

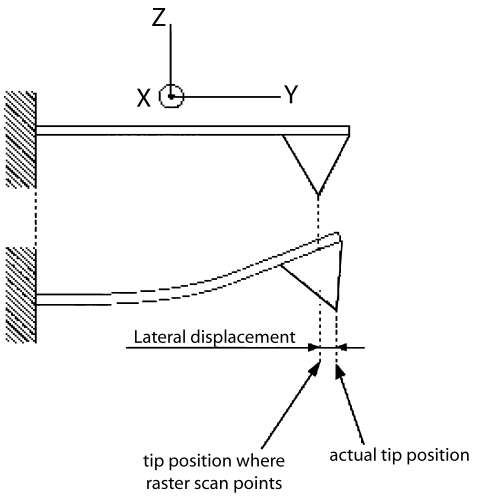

Fig. 5.6. Lateral displacement along Y direction, generated by the Z direction force [11]

when the load force is less than 10 nN [10]. At a greater load force viscous–flow-like deformation was observed [26]. Tip sliding causes torque motion and this motion contributes to the deflection and torsion of the cantilever in addition to displacement of the cantilever along the y direction. The ratio of the deflection component can be estimated from in situ measurements [10].

Shear behaviour in contacts was investigated in [27]. Figure 5.7 shows a time-sequence series of a shear deformation process in a gold contact. By shear displacement twinning occurs in the upper part (Fig. 5.7b) with subsequent twinning in the middle (Fig. 5.7) and lower parts (Fig. 5.7) when the tip is moved left. The twinning gradually recovers by displacement of the tip to the right and finally tips become a different single crystalline structure in comparison to Fig. 5.7. This shows that slip is also attributed to the deformation. A slip process with atomic resolution is visualized in Fig. 5.8

Stick slip motion was also observed when the gold tip is scanned over a gold surface with zero distance [27] (Fig. 5.9). This means that the displacement is disturbed by a kinetic friction. Several layers at the two surfaces and the contact boundary are responsible for the contact-type surface scanning process. The strength of the boundary is attributed to a static friction when two tips bond and fix and is responsible for a kinetic friction during the displacement.

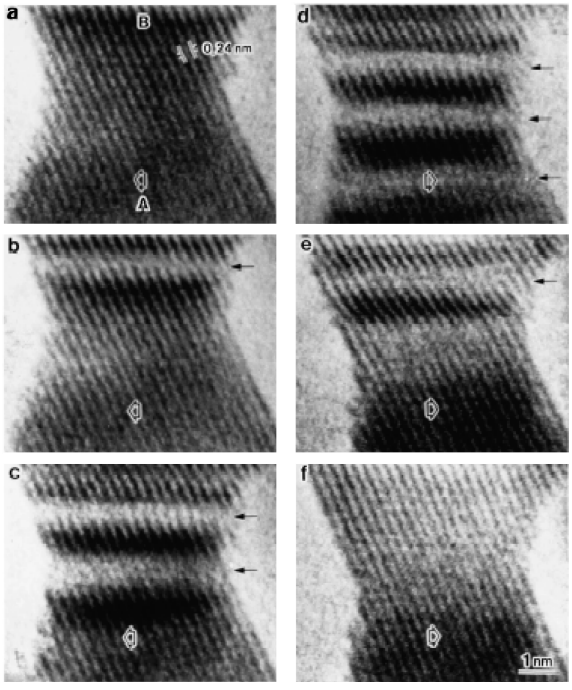

Fig. 5.7. Images of the process of shear tests in nanometer-sized gold. Bold arrays show the direction of displacement of the mobile side. Arrows show twinning [27]

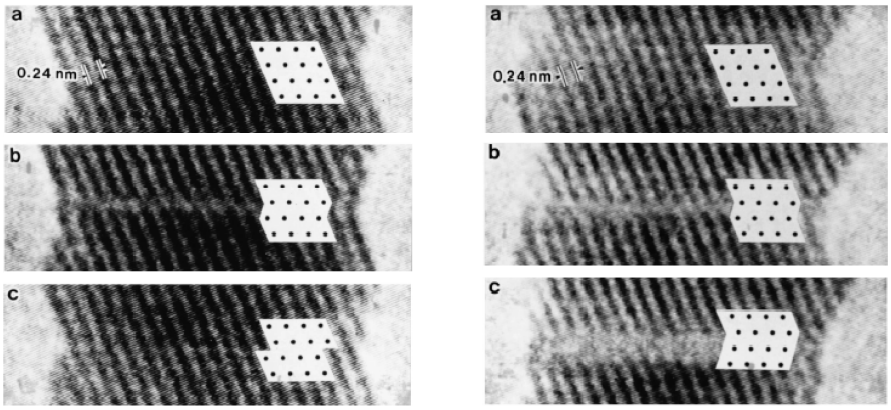

Fig. 5.8. Images of the process of slip (*left side column*) and twinning (*right side column*) during the shear deformation. An atomic arrangement projected along the [110] axis is inserted [27]

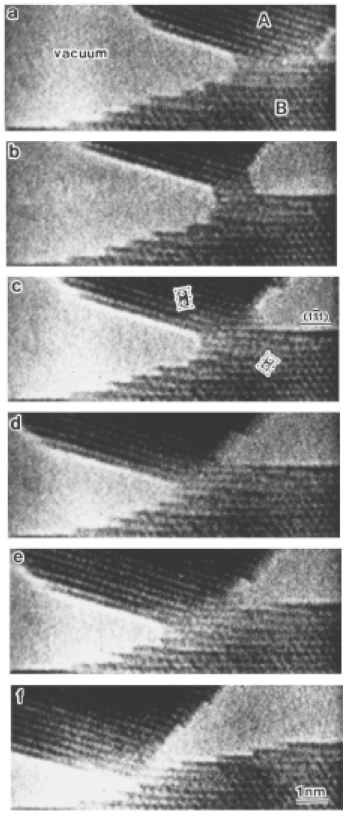

Fig. 5.9. Images of the scanning of a gold tip when the distance between the tip and a gold tip in a fixed side is 0 nm. The two tips bond by a boundary of a few atomic columns width. Frames show the unit cells of gold with face-centred cubic structure projected along the [110] direction [18]

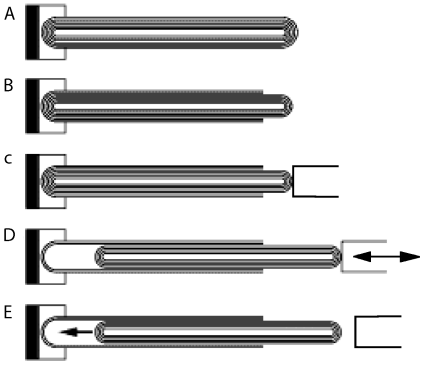

Fig. 5.10. Schematic representation of the experiments performed inside TEM. **A** to **C** The process of opening the end of MWNT (**A**), exposing the core tubes (**B**), and attaching the nanomanipulator to the core tubes (**C**). **D** and **E** Two different classes of subsequent experiments performed. In **D**, the nanotube is repeatedly telescoped while observations for wear are performed. In **E**, the core is relased and pulled into the outer shell housing by attractive van der Waals force [4]

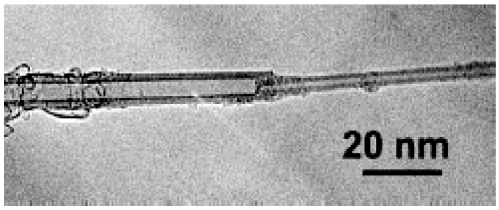

Fig. 5.11. A TEM image of a telescoped nanotube. This particular nanotube originally had nine shells, but upon telescoping a four shell core has been nearly completly extracted [4]

In [4] low friction nanoscale linear bearing from multiwall carbon nanotubes was realized as shown in schematics in Figs. 5.10 and 5.11. The manipulator is contacting to the inner shells of nanotube and controlled and reversible telescoping of inner shells according to outer shells is realized. After 20 telescopic processes with different nanotubes no evidence for sliding induced wear on active surfaces was found. Telescopic nanotube is expected to act as constant force spring and the telescoped part is moving back by vander Waals driven forces. Static and dynamic friction forces are calculated.

5.3.4 Electrostatic forces

Force curves can be changed by applying an electrical field between the surface and the tip. Electrostatic forces have been investigated between Si and Ge nanowires and a gold electrode in [21] and carbon nanotube bundles [28]. In [29, 30] electrostatic forces between the electrode and a carbon nanotube were used for exiting carbon nanotubes to resonance frequencies and determination of the Young modulus.

Forces acting on a Ge nanowire – gold tip (Fig. 5.12a) are schematically shown in Fig. 5.12b. Figure 5.12c shows the comparison between the calculated and measured forces for the interactions between a Si nanowire – gold electrode at a bias of 1 V. There is good agreement with the experimental results of the jump-to-contact and jump-off-contact distance at low voltages. Higher voltages tend to result in longer jump-to-contact and shorten jump-off-contact distances than calculated. This suggests that the electrostatic at-

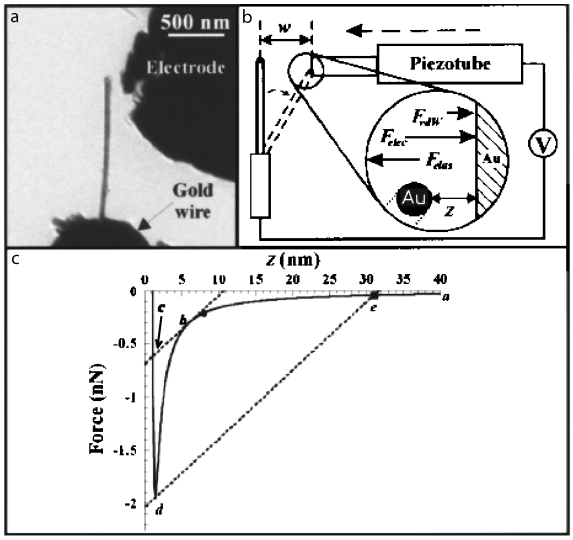

Fig. 5.12. a TEM image of a Ge nanowire utilized for TEM-STM measurements. **b** Schematic representation of TEM-STM studies. The electrode is positioned by movement of the piezotube. The zoom-in picture demonstrates the force interactions between the nanowire tip and the electrode where z is the distance of separation between the nanowire tip and the electrode with w being the initial separation distance. The attractive vdW (F_{vdW}) and electrostatic (F_{elec}) forces are countered by the elastic force exerted by the nanowire (F_{elas}). With applied electrostatic voltages, the total force acting on the nanowire tip is $F_{\mathrm{T}} = F_{\mathrm{vdW}} + F_{\mathrm{elec}}$. **c** Force-distance plot calculated for the interactions of a Si nanowire ($d = 90\,\mathrm{nm}$) with an applied voltage of 1 V. The dotted lines represent the spring constant of the nanowire. Measured jump-to-contact (*circle*) and jump-off-contact (*square*) distances are plotted for comparison [21]

tractive interaction forces are stronger than the sphere-plane interactions calculated at high potentials which could be due to the breakdown of the electrostatic potential equation at high voltages or large distances. Movement of the nanowire during withdrawal results in shearing forces at the contact point and shorter jump-off-contact distances are observed.

Electrostatic force driven jump-to-contact from a distance of 30 nm was observed between carbon nanotube bundles [28]. Forces acting on the nanowire were calculated by a capacitator model but were not directly measured.

Electrostatic forces are applied for the realization of fast nanoelectromechanical devices. The switching behaviour of a bistable nanowire-based nanoelectromechanical erasable programmable read-only memory (NEMPROM) device is shown in Fig. 5.13. It can be seen by the calculated energy diagrams in Fig. 5.13a, there are two local minima at low voltages and the circuit is OFF due to an energy minimum at the device separation distance (w) where the elastic energy of the nanowire is zero. The other minimum is due to van

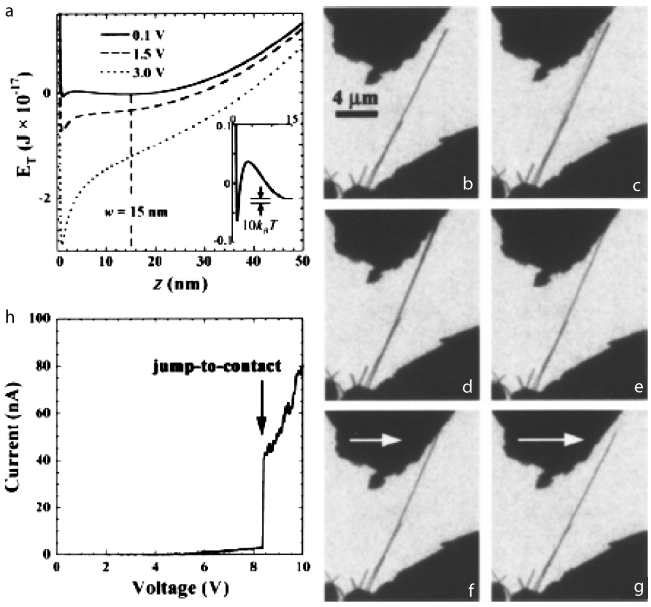

Fig. 5.13. a NEMPROM device calculations at different electrostatic potentials for Ge nanowire ($d = 50\,\text{nm}$; $l = 1.5\,\mu\text{m}$). Inset shows the energy barrier between two stable (ON/OFF) minima in relation to $10\,k_\text{B}T$. **b–d** TEM sequence showing the jump-to-contact of a Ge nanowire as the voltage is increased. **e** TEM image demonstrating the stability of device after removal of the electrostatic potential. **f,g** The resetting behaviour of the device. Note that the device is indefinitely stable but reset with the slight amount of shearing motion. **h** I(V) of NEMPROM device showing no conductivity until after contact is made at a potential of 8.4 V [21]

der Waals interactions when the wire and electrode are in contact. To switch between these two minima, an electrostatic field of 3 V is applied which alters the interaction energy resulting in a new energy minimum at shorter separation distances and deflection of the nanowire into contact with the gold electrode resulting in an ON state. Removal of the electrostatic potential does not allow the nanowire to switch to the OFF position due to the energy barrier and is stable when the barrier $\gg 10k_\text{B}T$. An NEWPROM device made from a Ge nanowire can be seen in the TEM sequence shown in Fig. 5.13b–f. By applying a voltage, the resulting electrostatic field deflects the nanowire into contact with the gold electrode. The nanowire does not jump-to-contact until the attractive electrostatic potential is greater than the elastic potential energy of the nanowire. Figure 5.13h verifies that there is no conductivity until the jump-to-contact is made at 8.4 V. The nanowire remains in contact with the electrode even when the electrostatic field is removed due to the minimum in the potential energy curve. Although these devices are stable, these NEWPROM devices can be easily switched OFF by mechanical motion

or by heating the device above the stability limit ($\gg 10k_{\mathrm{B}}T$). Figure 5.13e through 5.13g demonstrates that very little shearing motion is required to overcome the van der Waals attractive forces.

5.4 Nanocontacts

5.4.1 Contact Formation

Using TEM-SPM as manipulator, contact formation between two tips can be observed. For example contact formation between gold surfaces [18,31] and Si surfaces coated with an oxide layer [32] and without an oxide layer [33] have been investigated with atomic resolution. For an Au tip approach to distance of 0.3 nm, a few atomic columns emerge (Fig. 5.14) and two tips are contacted with a boundary of a few atomic columns width [18, 31]. Atom diffusion at nanometer sized contacts occurs due to the decrease in barrier height in addition to atomic force, and/or atomic emission in an electric field [31]. Material jump in contact between gold nanoasperities was also observed from larger distances of 0.9 – 1 nm (Fig. 5.15) [34]. This distance is two times larger than the value obtained by molecular dynamics simulations by Landman et al. [35].

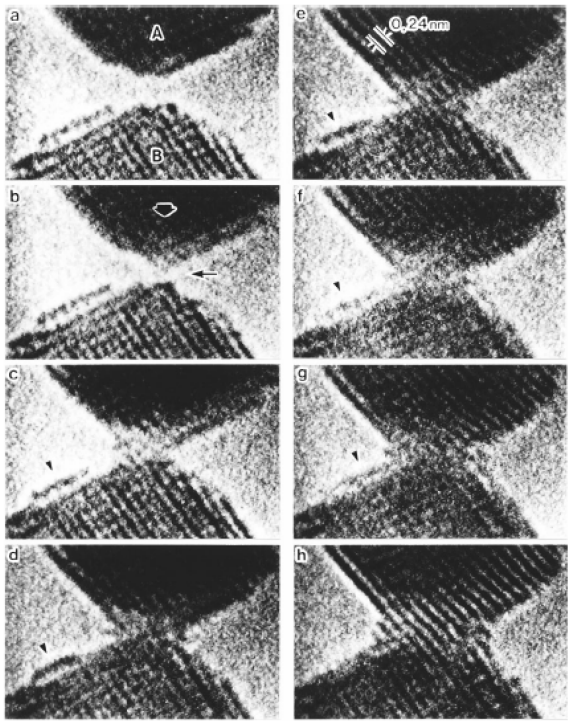

Fig. 5.14. Images of the formation of contact boundary and neck growth in the point contact of gold [31]

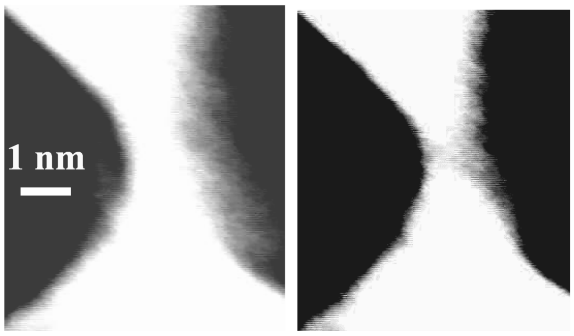

Fig. 5.15. Gold bride organization between two nanoasperities at distance around 1 nm [34]

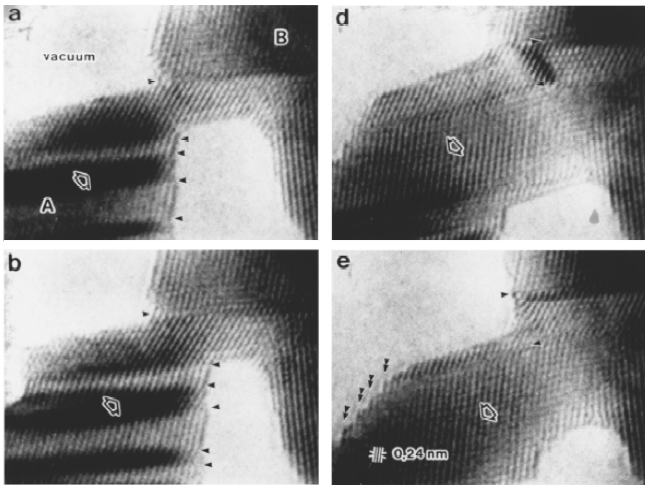

Fig. 5.16. Images of the process of compressing and tensile deformation in nanometer-sized gold. Bold arrays show the direction of displacement of the mobile side. Triangles show {111{/{111} $\Sigma = 3$ twin boundaries. Double triangles show atomic-scale slip steps [27]

By tip movement further growth of the diameter of the neck occurs due to the compressive deformation and contribution of gold surface diffusion [31]. By contact compression twin boundaries (the bright bands between the dark bands are twins) are generated, migrated, and annihilated [27] (Fig. 5.16a–c).

Figure 5.17 shows contact formation by pressing together two Si tips coated with amorphous oxide coated silicon with a thickness of 2 nm [32]. The contact boundary is located in the centre of amorphous interphase layer. For contact between clean Si surfaces elastic deformation occurs near the contact boundary [33]. Contacts created are shown to be crystalline (Fig. 5.18). Depending on tip orientations and the mismatch angle, the tip rotation and defect formation is observed at the contact boundary (Fig. 5.18). The defect formation shows that atomic diffusion to annihilate defects does not occur at

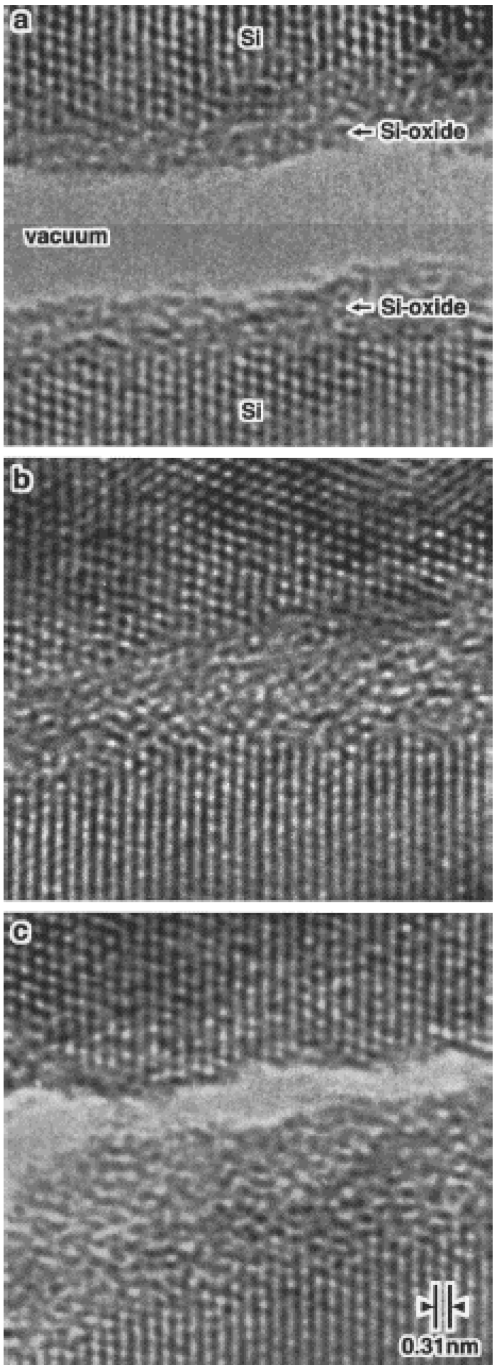

Fig. 5.17. Images of contact and the subsequent retraction process of two Si tips coated with amorphys Si oxide of about 1 nm thickness [32]

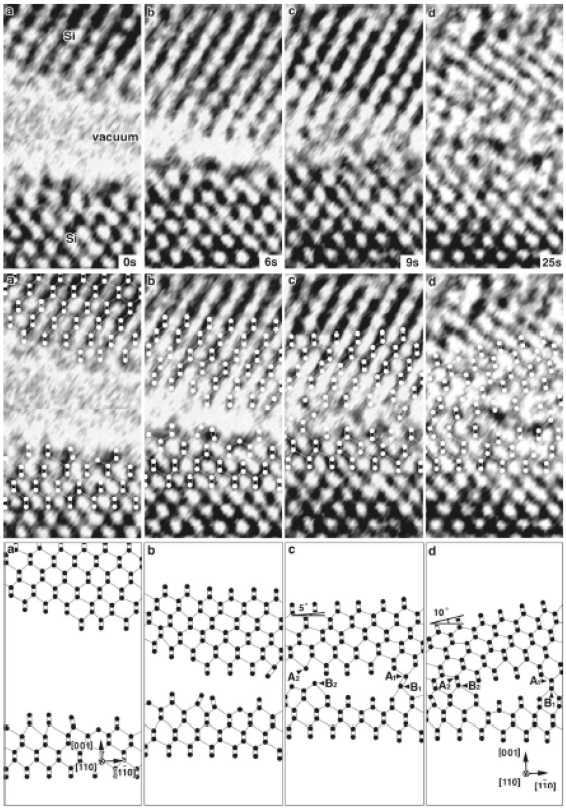

Fig. 5.18. TEM image of Si surfaces before in situ contact and after. White filled circles and lines show the positions of the atomic columns along [110] and Si–Si atomic bonding, respectively [33]

room temperature. In the gold contacts, contact boundaries are relaxed due to atomic diffusion at room temperature; localized defect structures including dislocations are not stable in the gold contact boundaries [31].

5.4.2 Contact breaking

TEM-SPM has been used to investigate contact behaviour under tensile stress for gold, silicon, and carbon nanotubes [2,4,27,32]. When large gold contacts are deformed by tensile force (Fig. 5.16) twin boundaries are generated, migrated, and annihilated [27] (Fig. 5.16c–f) similar to that seen during contact compression (Fig. 5.16a–c). Slip steps on an atomic scale form edges (shown by triangles in Figs. 5.16a–c) even twin boundaries are not observed. This shows that slip is also attributed to the deformation. Stick slip motion and stacking fault formation were investigated together with measurements of tensile stress and strain-stress curves in [10]. It was shown that between slips the point contact is deformed elastically. Structural relaxation due to atomic flow is observed after the slip particularly when the width of the point contact is less than 1 nm [31].

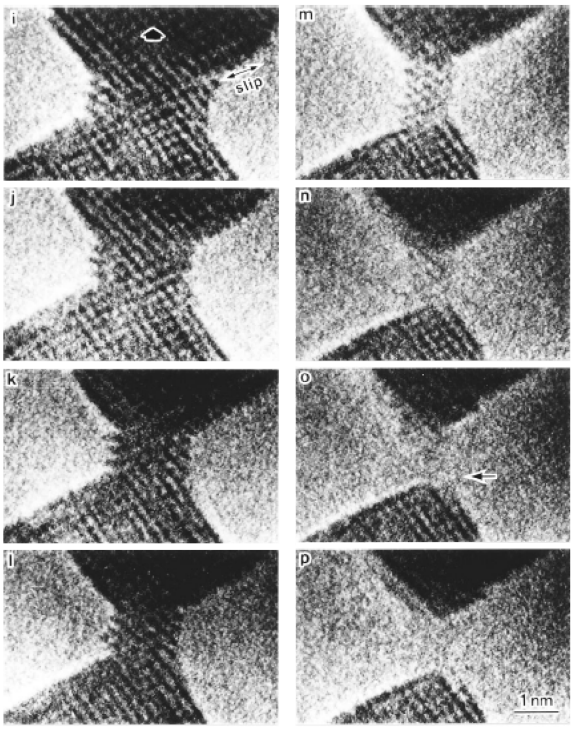

Fig. 5.19. Images of the formation of an atomistic pillarlike neck of gold during retraction. The width of the pillarlike neck is shown by the number of the (002) atomic layers in upper tip (A); the numbers is 14 (**i**), 11 (**j**), 9 (**k**), 8 (**l**), and 5 (**m**) [31]

The formation of atomistic pillar like necks by the slip deformation and structural relaxation during retraction was observed by [31] (Fig. 5.19). During the fracture and disappearance of such necks the introduction of a dislocation or dislocation-like localized strain is could not be confirmed. Finally pillar like neck breaks and disappears. The shape of tips becomes sharp as compared with that before contact. The top of the tips elongates by a few atomic layers after contact breaking.

Figure 5.20 demonstrates the breaking gold contact diameter from only a 6 atom line to 1 atom line [2]. It can be seen that the gold chains break one by one. The distance between individual atoms in the last gold atom chain is larger in comparison to gold atomic distances (Fig. 5.21).

The contact between oxidized Si surfaces and the amorphous interphase layers is viscously elongated during retracting and the crystalline Si regions are also deformed (Fig. 5.17) [32]. No slip of the lattices or dislocation motion was observed during the deformation in the crystalline regions and they deformed elastically not plastically. The bonding boundary is fractured at the boundary between the amorphous Si oxide and the crystalline Si (Fig. 5.17c). The thickness of the amorphous layer along the retraction direction increases by about 1 nm due to a viscous flow-like deformation. Such deformations were observed for surfaces with other orientations.

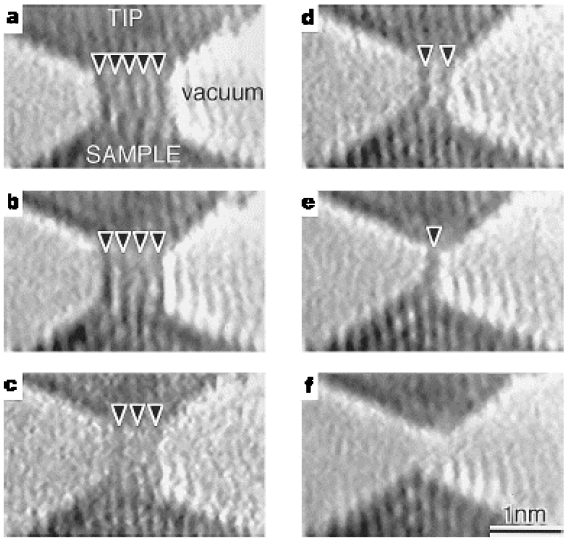

Fig. 5.20. Images of a contact while withdrawing the tip. A gold bridge thinned from **a** to **e** and ruptured at **f**. Dark lines indicated by arrowheads are rows of gold atoms. The conductance of the contact is 0 at **f** and in units of quantum conductance $\approx (13\,\mathrm{k\Omega})^{-1}$ at $V = -10\,\mathrm{mV}$, $R = 10\,\mathrm{k\Omega}$ [2]

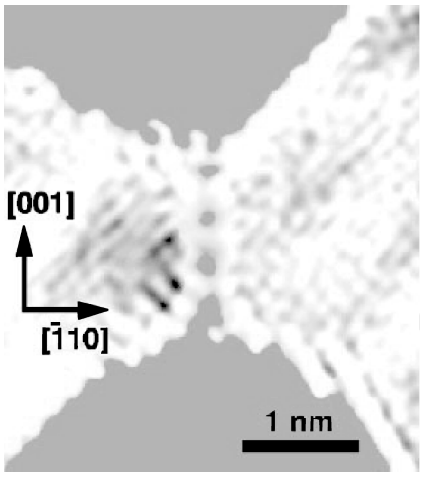

Fig. 5.21. Image of a linear strand of gold atoms (four colored dots) forming a bridge between two gold films (colored areas). The spacings of the four gold atoms are 0.35 – 0.40 nm. The strand is oriented along the direction of the gold (110) film. This image was processed to highlight the linear strand, where the lattice fringes of the gold film in the original electron microscope image were filtered out by Fourier transform [2]

Stretching and breaking weaker contacts formed by nanoparticle chain aggregates composed of carbon, titanium, alumina, and iron oxide have been performed by [16,36] using a breaking device inside a TEM. Figure 5.22 shows one example of stretching, breaking and recoiling of such chains observed in situ.

5.4.3 Adhesion

In [9] TEM-AFM was used to compare adhesion theories. The contact area between two gold electrodes was measured by a zero applied load when the contact area is determined by adhesion forces only. At zero loads it is not

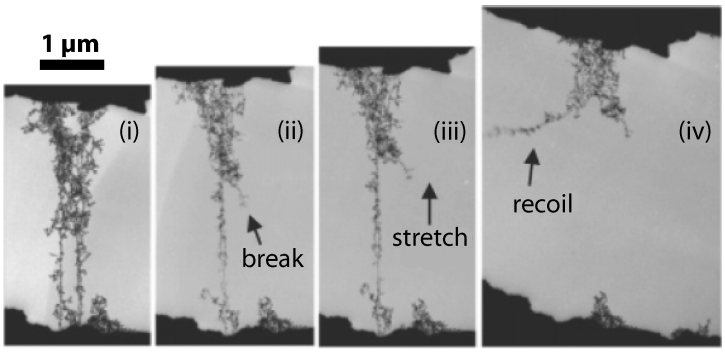

Fig. 5.22. TEM photo showing the sequential stretching and breaking of single nanoparticle chain aggregate (NCA) chains: **i** NCA deposited between two separating surfaces; **ii** stretching and breaking of one of the chains; **iii** stretching and **iv** breaking of second chain. The lower broken part disappeared, probably because it recoiled to the specimen support. In both **ii** and **iv**, the chain broke somewhere along its length and did not detach at the support surfaces [36]

necessary to know the cantilever spring constant and uncertainties in the cantilever force constant are not important.

The limiting cases in contact adhesion are based on Johnson–Kendall–Roberts (JKR) [37], Derjaguin–Müller–Toporov (DMT) [38] theories, and the transition between them, can be described by a dimensionless transition parameters called the Tabor parameter μ [39] and the Maugis parameter λ [40]. Both parameters are related and for contact between identical materials can be expressed as:

$$\lambda = 1.157\mu = \left(\frac{64R\gamma^2}{9K^2 z_0^3}\right)^{\frac{1}{3}}, \tag{5.2}$$

where z_0 is a typical atomic dimension, γ is surface energy and the reduced Young modulus K is given by $K = 4/3((1-\nu_1^2)/E_1 + (1-\nu_2^2)/E_2)^{-1}$, where ν_1 and ν_2 are Poissons ratio and E_1 and E_2 are Young modulus for two contacting spheres.

The DMT theory is valid when $\mu < 0.1$ and the JKR theory is valid when $\mu > 5$. Maugis [40] provides a more general theory suitable for the full range, where λ is a transition parameter. A dimensionless contact radius at zero applied loads, $\breve{\alpha}_0$ is described by:

$$\breve{\alpha}_0(\lambda) = \alpha_0 \frac{K}{2\pi\gamma R^2}^{\frac{1}{3}} \text{ TS}^{\text{g}}, \tag{5.3}$$

where α_0 is the real contact radius. Maugis solution is analytical, but here we use a simplified fitting version given by Carpick et al. [41]:

$$\breve{\alpha}_0(\lambda) = 1.54 + 0.279\left(\frac{2.28\lambda^{1.3} - 1}{2.28\lambda^{1.3} + 1}\right). \tag{5.4}$$

TS$^{\text{g}}$ Parentheses missing? Or check position of exponent.

Editor's or typesetter's annotations (will be removed before the final TEX run)

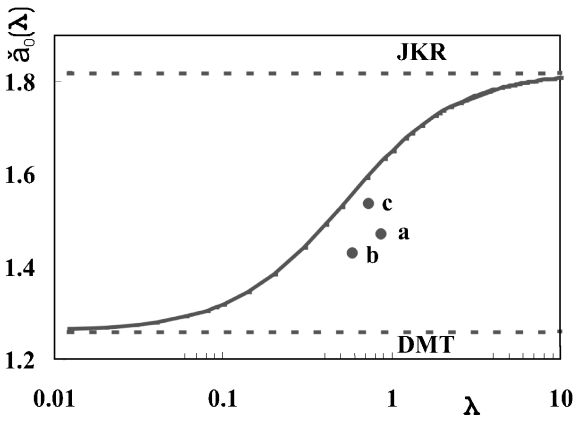

Fig. 5.23. Dimensionless contact radius at zero applied load for three contacts: **a** corresponds to the contact in Fig. 5.2, **b** and **c** are not shown). The solid line is the Maugis theory (Eq. 5.4) and the JKR and DMT limits are shown with dotted lines. Reproduced with permission from *Appl. Surf. Sci.* **2002,** 188, 460, Copyright 2002 Elsevier North-Holland

To calculate λ (and μ), the following values for gold were used: $\gamma = 1.37\,\mathrm{J/m^2}$ [42], $E = 117\,\mathrm{GPa}$, $\nu = 0.42$ [43], $z_0 = 0.28\,\mathrm{nm}$. These values are dependent on the lattice orientation and the reported values in the literature have a spread of up to 50%, which could change the picture quite a bit. The theoretical and experimental values of the contact radius at zero applied loads are shown in Fig. 5.23. Our experimental results were in the transition region between the DMT and JKR models.

This TEM-AFM method, if extended to include the critical load, could mean that this question could be addressed experimentally in an adequate way. In this way one could measure γ independently, and arrive with a safer λ.

5.5 Conductivity of Nanocontacts

Analysis of conductivity dependence on contact size by TEM-STM was the main task in the beginning leading to the invention of the TEM-SPM. [2, 5, 10]. Previously conductivity quantization was observed by different contact breaking techniques, for example, STM and break junctions where the main problem was the real observation of contact size. The TEM-SPM technique gives clear verification that conductivity quantization occurs for contacts with atomic dimensions. Conductivity for last atom chain as shown in Fig. 5.20 is equal to $2 \times 13\,\mathrm{k\Omega}$ where $13\,\mathrm{k\Omega}$ corresponds to the quantum resistance $R_e = h/2e^2$ [44], where h is Plank constant and e is electron charge. Figure 5.24 shows the same figure in conductivity units (Fig. 5.24a) and schematics of the atom arrangements just before breaking (Fig. 5.24d)

In [5] conductivity was also measured for larger sized gold nanocontacts and results were compared with the Sharvin [45] and Wexler [46] theories. It was shown that ballistic electron transport is observed for gold nanowires with diameter around 1 nm (straight line in Fig. 5.25). At larger diameters experimental points were fitted with the Wexler formulae for the mixed

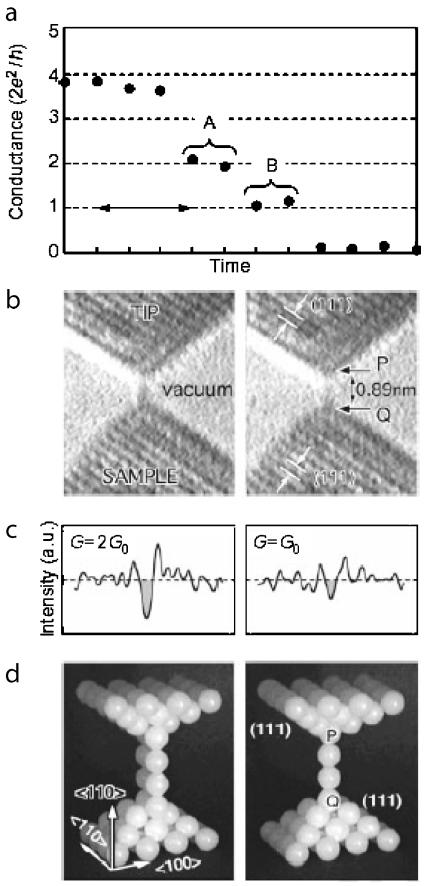

Fig. 5.24. Quantized conductance of a single and double strand of gold atoms. **a** Conductance change of a contact while wuthdrawing the tip. Conductance is shown in units of quantum conductance $G_0 = 2e^2/h \approx (13\,\mathrm{k\Omega})^{-1}$. $V = 13\,\mathrm{mV}$, $R = 100\,\mathrm{k\Omega}$. **b** images of gold bridges obtained simultaneously with the conductance measurements in (**a**). Left bridge at *step A*; right bridge at *step B*. **c** Intensity profiles of the left and right bridges shown in (**b**). The shaded area is the intensity from the bridge after subtraction of the background noise. **d** Models of the left and right bridges. The bridge at *step A* has two rows of atoms; the bridge at *step B* has only one row of atoms. The distance from P to Q (see **b**) is about 0.89 nm, wide enough to have two gold atoms in a bridge if the gold atoms have the nearest-neighbour spacing of the bulk crystal (0.288 nm) [2]

Sharvin-Maxwell regime. From this data, the electron mean free path was calculated and it was found to be only 4 nm which is 10 times lower in comparison to bulk gold and can be explained by the presence of defects in the gold nanowires [5].

Recently TEM-SPM was also used to determine conductivity through individual nanowires and carbon nanotubes. The $I(V)$ characteristics of Si and Ge nanowires indicated that ohmic contacts could be made with silicon nanowires whereas germanium nanowires displayed $I(V)$ that were dependent on the point of contact (Fig. 5.26) [21]. The observed nonconductive gaps in $I(V)$ characteristics for Ge nanowires were explained by the presence of different thickness oxide layers on the nanowires.

Although the contact resistances cannot be adequately determined, it was found that the resistivities of the Si nanowires were approximated in the order of $10^{-2}\,\Omega\,\mathrm{m}$ which are indicative of a highly doped nanowires with an impurity (most probably gold).

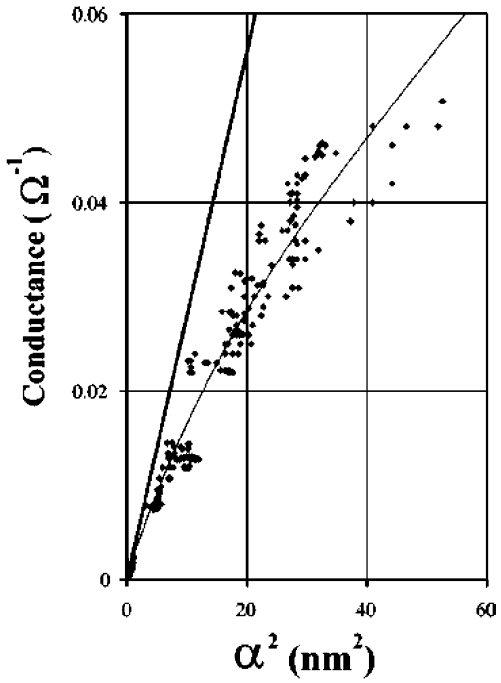

Fig. 5.25. Measured point contact conductance (Ω^{-1}) vs. radius squared (α^2), at bias 10 mV. The Wexler interpolation formula is plotted using a mean free path value of 3.8 nm and $\Gamma = 0.7$. Sharvin conductance (*straight thick line*) is added for comparison. Reproduced with permission from *Phys. Rev. B* **2000**, 61, 12725, Copyright 2000 American Physical Society

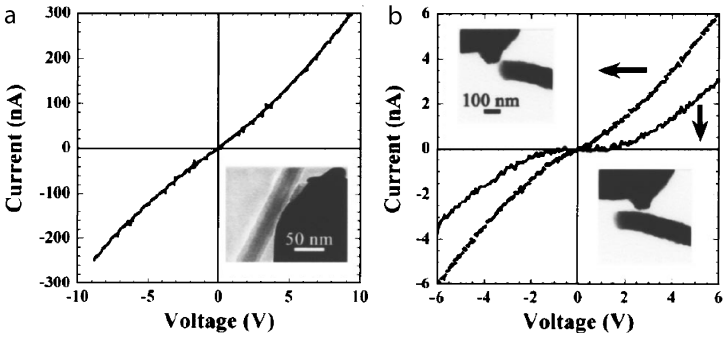

Fig. 5.26. I(V) behavior for an individual **a** Si and **b** Ge nanowire. I(V) for Ge nanowires are contact dependent [21]

For precise measurements of conductivity in carbon nanotubes in [47] contacts with liquid metal surface are created and contact resistances in the range 0.1 to 1 kΩ µm were obtained. Ballistic electron transport in carbon nanotubes was measured and an electron mean free path longer than 65 µm was found in the nanotubes.

Resistivity between the ends of multiwall carbon nanotubes during telescopic extension of the nanotube was investigated in [48]. Nonlinear resistance between the ends of the multiwall nanotubes during telescopic extension of

nanotube was observed and a one-dimensional localized system with characteristic localization length 1000 – 1500 nm predicted.

Besides conductivity TEM-STM can be applied for the characterization of tunnelling and field emission. Field emission properties of boron nitride and carbon nanotubes were measured in situ by Zettl [49] and our groups. Current-voltage characteristics were measured and work-function determined. In [50] electron holography of carbon nanotubes has been performed in situ. This method gave information about inner electric fields of materials. Measurements of the phase shift and phase gradient maps (Fig. 5.27) show that the electric field is concentrated precisely at the end of nanotubes and not at other nanotube defects such as sidewall imperfections.

One specific topic in conductivity measurements is contact behaviour under high current densities which can be achieved by relatively low bias voltages. By applying voltage between the graphite coated tip and graphite surface occasionally nanotube growth was observed (Fig. 5.28) [51]. It is shown that the bias voltage plays a key role in triggering the formation of

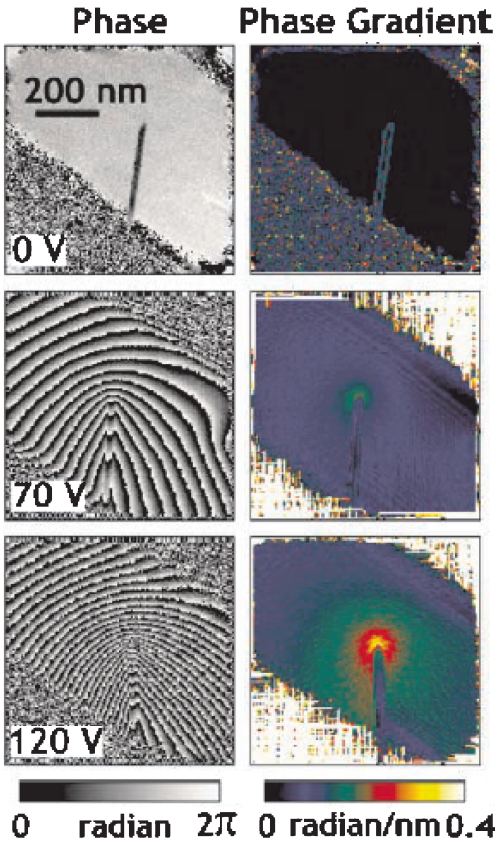

Fig. 5.27. Phase shift and phase gradient maps extracted from holograms of the same nanotube at bias voltages 0, 70, and 120 V. The phase gradient indicates where the electric field is the strongest; note the concentration of the electric field at the nanotube tip for 70 and 120 V [50]

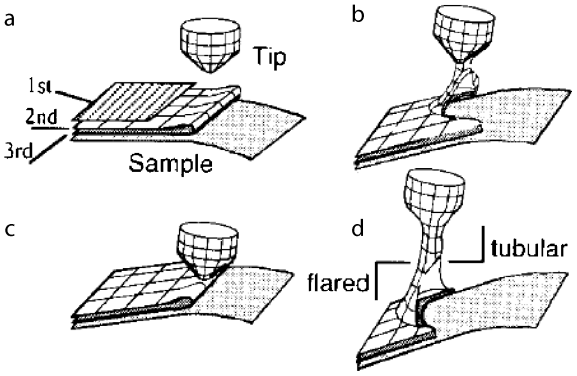

Fig. 5.28. Model of the growth of a nanobridge. **a** Before contact. **b** The tip touches edge. **c** The tip is retracted. **d** Nanotube growth by further retraction [51]

a nanobridge at the initial stage. The voltage can drive the formation through Joule heating which may achieve at least 3700 K at which rearrangements of graphite layer into hexagons, heptagons, and pentagons can be achieved. The tubular parts of the carbon bridges grow in length during the retraction of the tip which may be driven by Joule heating.

Welding of nanotubes to Au and Si surfaces was realized [25]. Thermal heating at a bias voltage in the range of 2 V is sufficient for contact formation with Au and 5 V with Si. Diffusion of Au into the nanotube interlayer is observed after bonding. Si and Au surface melting was observed in contact areas, which means that the temperature reaches at least 1687 K. In [28] welding of two carbon nanotube bundles was observed using bias voltages 2 – 3 V.

High current densities can be used for controlled nanotube cutting as was realized by contact with amorphous carbon. In each contact the cut part of the nanotube achieve 5 – 10 nm at a bias of 5 V [25].

5.6 Electromigration (or Material Transport)

Material transport in nanotubes [6] and on nanotube surfaces [7,52] has been observed. Electromigration forces, created at high electron current densities, have been shown to enable the transport iron inside carbon nanotubes [6] (Fig. 5.29).

In [7] carbon nanotubes were used for controllable, reversible atomic scale mass transport of indium metal along the nanotubes. Surface driven nanoelectromechanical relaxation oscillator has been proposed (Fig. 5.30) [52].

Recently nanocrystal powered nanomotors have been realized by using a nomanipulator inside a TEM (Fig. 5.31) [53]. Movement is achieved by applying an electric field.

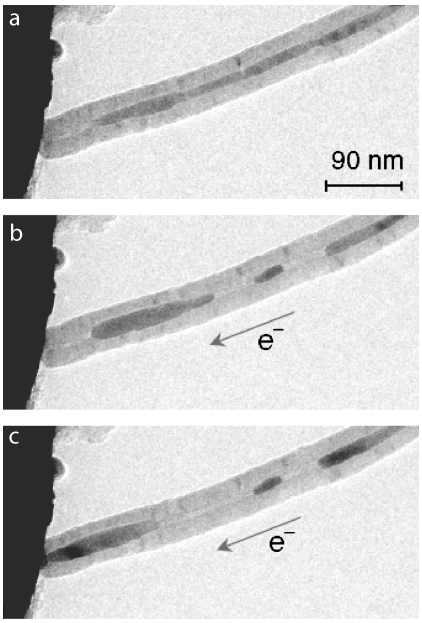

Fig. 5.29. Sequential TEM images showing the induced movement of iron inside carbon nanotubes at time **a** – 0, **b** – 2, **c** – 3 min. Iron migrates in the same direction as the electron flow [6]

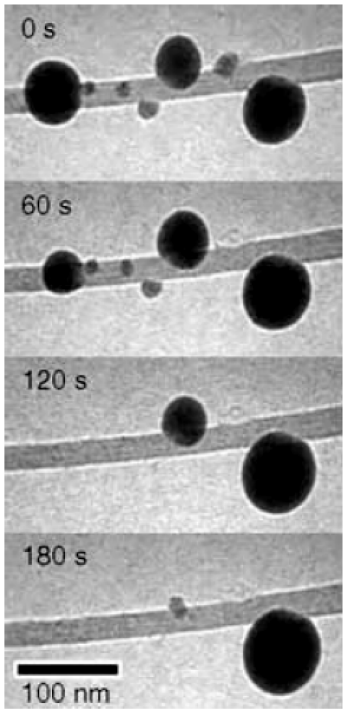

Fig. 5.30. Four TEM images, spaced by one-minute increments, left to right indium transport on a single MWNT [7]

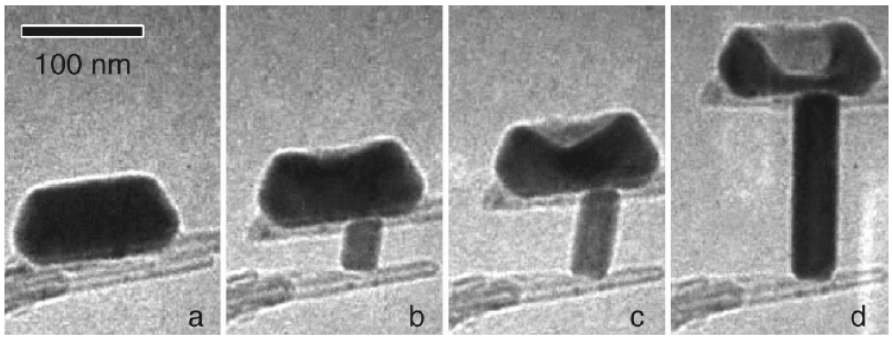

Fig. 5.31. Images showing nanocrystal ram extension. **a** Two multiwall nanotubes (MWNT) lie in contact with one another. A reservoir of indium atoms rests on the top nanotube. **b** Driving 2.1 μA through the circuit creates the nanocrystal ram, which begins to push the MWNT apart. **c** The nanocrystal ram has growth to 75 nm long. **d** At full extension the nanocrystal ram is more than 150 nm long [53]

5.7 Conclusions

The new methods of probing inside transmission electron microscopes have proved to be of use tool for investigation of nanocontacts. However, many of the examples discussed above only demonstrate the potential of in situ probing to address problems in nanotribology. There is one single parameter in friction that is of importance in almost all studies: the contact area, which is directly visible using the TEM-AFM. If future nanotribology work, using TEM-AFM, is contact area alone makes it an important new tool. Almost all AFM tribology studies done, except for the ones in liquid environments, can be repeated using in situ methods and will provide new information, and will more than ones be with unexpected results. For example be interesting to make more experiments along the original slip-stick experiment [18, 54], the force and conductance AFM measurements on atomic-scale metallic contacts [10,23], or studies of lubricated samples, for example the squeezing out of lubrication fluids between two surfaces [55]. The power of imaging the contacts in nanotribology experiments will, if pursued, give new insight to this interesting field. The power of imaging the contacts in nanotribology experiments will, if pursued, give new insight to this interesting field.

References

1. J.C.H. Spence: Ultramicroscopy 25, 165 (1988); J.C.H. Spence, W. Lo, M. Kuwabara: Ultramicroscopy 33, 69 (1990); W. Lo and J.C.H. Spence: Ultramicroscopy 48, 433 (1993)
2. H. Ohnishi, Y. Kondo, K. Takayanagi: Nature 395, 780 (1998)
3. P. Poncharal, Z.L. Wang, D. Ugarte, W.A. de Heer:Science 283, 1513 (1999)

4. J. Cumings and A. Zettl: Science 289, 602 (2000)
5. D. Erts, H. Olin, L. Ryen, E. Olsson, A. Thölén: Phys. Rev. B 61,12725 (2000)
6. K. Svensson, H. Olin, E. Olsson: Phys. Rev. Lett 93, 14590 (2004)
7. [Zetl_Nature04] B.C. Regan, S. Aloni, R.O. Ritchie, U. Dahmen, A. Zettl. Nature, 428, 924 (2004)
8. D. Erts, A. Lõhmus, R. Lõhmus, H. Olin: Appl. Phys. A 72, 71 (2001)
9. D. Erts, A. Lõhmus, R. Lõhmus, H. Olin, A.V. Pokropivny, L. Ryen, K. Svensson: Appl. Surf. Sci. 188, 460 (2002)
10. T. Kizuka, H. Ohmi, T. Sumi, K. Kumazawa, S. Deguchi, M. Naruse, S. Fujisawa, S. Sasaki, A. Yabe, Y. Enemoto: Jpn. J. Appl. Phys. 40 (2001) L170
11. S. Fujisawa and T. Kizuka: Tribol. Lett. 15, 163 (2003)
12. A.M. Minor, E.A. Stach, J.W. Morris: Appl. Phys. Lett. 79, 1625(2001)
13. A. Nafari, P. Enoksson, H. Olin, A. Danilov, and H. Rödjegrd: Sens. Actuators A 123-124, 44 (2005)
14. M.S. Bobji, J.B. Pethica, B.J. Inkson: J. Mat. Res. 20, 2726 (2005)
15. Nanofactory Instruments, www.nanofactory.com
16. Y J. Suh, S.K. Friedlander: J. Appl. Phys. 93, 3515-3523]
17. M.I. Lutwyche, Y. Wada: Sens. Actuators, A 48, 127 (1995)
18. T. Kizuka, K. Yamada, S. Degushi, M. Naruse, N. Tanaka: Phys. Rev. B 55, R7398 (1997)
19. K. Svensson, Y. Jompol, H. Olin, E. Olsson: Rev. Sci. Instr. 74, 4475 (2003)
20. A. Debarre,A. Richard, Techenio: Rew. Sci. Instrum, 68, 4120 (1997).
21. K.J. Ziegler, D.M. Lyons, J.D. Holmes, D. Erts, B. Polyakov, H. Olin, K. Svensson, E. Olsson: Appl. Phys. Lett., 84, 4074 (2004)
22. J.N. Israelachvili: *Intermolecular and surface forces* (2nd ed. Academic Press, Inc.: San Diego, CA 1992)
23. G. Rubio, N. Agrait, S. Vieira: Phys. Rev. Lett. 76, 2302 (1996)
24. S. Blom, H. Olin, J.L. Costa-Krämer, N. Garcia, M. Jonson, P.A. Serena, R. Shekhter: Phys. Rev. B 57, 8830 (1998); C.A. Stafford, D. Baeriswyl, J. Bürki: Phys. Rev. Lett. 79, 2863 (1997); D. Sánchez-Portal, E. Artacho, J. Junquera, P. Ordejón, A. Garcia, J.M. Soler: Phys. Rev. Lett. 83 3884(1999)
25. T. Kuzumaki, H. Sawada, H. Ichinose, Y. Horiike, T. Kizuka: Apl. Phys. Lett. 9, 4580 (2001)
26. T. Kizuka, K. Hosoki, S. Deguchi, M. Naruse: Mat. Sci. Forum 551, 304-306 (1999)
27. T. Kizuka: Phys. Rev. B 57, 11158 (1998)
28. H. Hirayama, Y. Kawaamoto, Y. Ohshima, K. Takayanagi: Appl. Phys. Lett. 79, 1169 (2001)
29. P. Poncharal, Z.L. Wang, D. Ugarte, W.A. de Heer: Science 283, 1513 (1999)
30. Z.L. Wang, R.P. Gao, P. Poncharal, W.A. de Heer, Z.R. Dai, Z.W. Pan: Mater. Sci. Eng. C 16, 3 (2001)
31. T. Kizuka: Phys. Rev. Lett. 81, 4448 (1998)
32. T. Kizuka, K. Hosoki: Appl. Phys. Lett. 75, 2743 (1999)
33. T. Kizuka: Phys. Rev. B 63, 033309 (2001)
34. R. Lõhmus, D. Erts, A. Lõhmus, A, Svensson K, Jompol, H. Olin: Phys Low-Dimens Str 3-4, 81 (2001)
35. U. Landman, W.D. Luedtke, N.A. Burnham, R.J. Colton: Science 248, 454 (1990)
36. W. Rong, A.E. Pelling, A. Ryan, J.K. Gimzevski, S.K. Friedlander: Nano Lett. 4, 2287 (2004).

37. K.L. Johnson, K. Kendall, and A.D. Roberts: Proc. Roy. Soc. London A 324, 301 (1971)
38. B.V. Derjaguin, V.M. Muller, Yu.P. Toporov: J. Colloid Interface Sci. 53, 314 (1975)
39. D. Tabor, R.H.S. Winterton: Proc. R. Soc. London Ser. A 312, 435 (1975)
40. D. Maugis. J. Colloid Interface Sci. 150, 243 (1992)
41. R.W. Carpick, D.F. Ogletree, M. Salmeron: J. Coll. Interf. Sci. 211, 395 (1999)
42. D. Maugis: *Contact, Adhesion and Rupture of Elastic Solids* (Springer: Berlin 2000)
43. N. Agrait, G. Rubio, S. Vieira: Langmuir 12, 4505 (1996)
44. R. Landauer: IBM J. Rev. Dev. 1, 223 (1957)
45. Y.V. Sharvin: Zh. Exp.Teor. Fiz 48, 984, [Sov. Phys. JETP 21, 655 (1965)
46. G. Wexler. Proc. Phys. Soc. London, 89, 927 (1966)
47. P. Poncharal, C. Berger, Y. Yi, Z.L. Wang, W.A. de Heer: J. Phys.Chem. B 106, 12104 (2002)
48. J. Cumings, A. Zettl: Phys. Rev. Lett. 93, 086801-1 (2004)
49. J. Cummings, A. Zettl: Sol. St. Communications 129, 661-664 (2004)
50. J. Cumings, A. Zettl: Phys. Rev. Lett. 88, 056804-1 (2002)
51. J. Yamashita, H. Hirayama, Y. Ohshima, K. Takayanagi: Appl. Phys. Lett. 74, 2450 (1999)
52. B.C. Regan, S. Aloni, K. Jensen, A. Zettl: Appl. Phys. Lett. 86, 123119 (2005)
53. B.C. Regan, S. Aloni, K. Jensen, R.O. Ritchie, A. Zettl: Nano Lett. 5, 1730 (2005)
54. C.M. Mate, G.M. McClelland, R. Erlandsson, S. Chiang: Phys. Rev. Lett. 59, 1942 (1987)
55. B.N. Persson: Surf. Sci.Rep. 33, 85 (1999)